



A SARIMA-RVFL hybrid model assisted by wavelet decomposition for very short-term solar PV power generation forecast

Vishal Kushwaha*, Naran M. Pindoriya

Indian Institute of Technology Gandhinagar, Gujarat, India

ARTICLE INFO

Article history:

Received 23 July 2018

Received in revised form

1 February 2019

Accepted 5 March 2019

Available online 8 March 2019

Keywords:

Artificial neural network

Feature selection

Forecasting

Hybrid model

Solar PV power

Wavelet transform

ABSTRACT

A very short-term solar PV power generation forecast can be extremely helpful for real-time balancing operation in an electricity market which in turn will profit both energy suppliers as well as customers. However, the intermittency of solar PV power introduces inaccuracies in its forecast. To address this challenge, the research paper has studied the effect of wavelet decomposition of solar PV power time series on its forecast. A novel and time adaptive, Seasonal Autoregressive Integrated Moving Average (SARIMA)-Random Vector Functional Link (RVFL) neural network hybrid model assisted by Maximum Overlap Discrete Wavelet Transform (MODWT) has been proposed. The solar PV power generation data obtained from roof-top solar PV plants installed at IIT Gandhinagar is used to develop and validate the forecast models. Various numerical forecast accuracy measures have been calculated which show an improvement in accuracy and adaptability of proposed forecast model over constituent models.

© 2019 Elsevier Ltd. All rights reserved.

1. Introduction

Solar photovoltaic is one of the most popular forms of renewable energy throughout the world. The worldwide installed capacity of solar PV amounts close to 303 GW according to Ref. [1]. As of end-2016, China, Japan, Germany, United States and Italy are the top five countries of world in terms of total solar PV capacity/generation. In 2016, 76 GW of solar PV capacity was installed, which was a significant growth of 50% in the market [2]. This suggests that the penetration of solar PV will continue to increase in the coming future.

However, the solar PV power output depends on the ambient weather conditions such as incident solar radiation, temperature, humidity etc. As the weather parameters are themselves quite uncertain, the solar PV power also becomes uncertain in nature. Other factors like dust deposition on PV panels and gradual aging of PV systems add to the variability of the power output. This intermittent nature of solar PV power makes it non-dispatchable in nature. Therefore accurate values of solar PV power forecast can help power system operators to maintain the balance between power generation and demand thus maintaining stability in the grid.

The solar PV power forecast can be classified into following

categories depending on the forecast horizon [3]:- very short-term - few seconds to minutes ahead, short-term - one to three days ahead, medium-term - one week ahead and long-term - months to year ahead.

The authors have attempted very short-term solar PV power forecasting. Some of the key benefits associated with it are [4]:

- (1) There is always a deviation between the actual and scheduled generation in an electrical energy market. Therefore market operator has to perform real-time balancing operation. This is achieved by real-time imbalance energy market which operates in very short-term duration [5]. If an accurate forecast is available then solar PV plant owners can bid more accurately into the market to increase the revenue.
- (2) The market participants have to incur a penalty if there is large deviation between the actual and scheduled power generation. An accurate forecast can help in reducing such penalties as the bids become more strategic. In addition to this, they can plan maintenance stops in a better manner as well.
- (3) It can also indirectly aid in load forecasting. As most of the solar PV plants integrated into the distribution networks are behind the meter so a local power supply is interpreted as a reduction in demand by the grid operators. This causes appreciable errors in the load forecast. Thus solar PV power forecast can effectively help in improving the accuracy of the load forecast.

* Corresponding author.

E-mail addresses: VISHALKUSH9456@gmail.com (V. Kushwaha), naran@iitgn.ac.in (N.M. Pindoriya).

- (4) There will be an increase in reliability, stability and power quality of the grid. Also, the curtailment of solar PV power can be reduced. As a whole, the integration of solar PV systems into the existing grid will increase.

1.1. Forecast model classification

Different types of forecasting models have been reported in the literature. The past values of solar PV power generation can be used to determine the future values as they contain the information regarding trend and seasonality of the time series. Examples of these type of models are autoregressive (AR) model, moving average (MA) model, autoregressive integrated moving average (ARIMA) model [6], seasonal autoregressive integrated moving average (SARIMA) model, artificial neural network (ANN) [7] etc.

Use of weather parameters can increase forecast accuracy if properly taken into consideration. Such an approach requires the determination of functional relationship between the weather parameters and solar PV power generation. The forecast of weather parameters is provided by weather agencies which can be used as an input for the already determined functional relationship. Apart from the weather parameters, the input can contain past values of solar PV power time series as well. Examples of such models are ANN, autoregressive moving average with exogenous inputs (ARMAX) model, Support Vector Regression (SVR) [8], Adaptive Neuro Fuzzy Inference System (ANFIS) [9], Gaussian Process Regression (GPR) [10] etc. For proper working of these models, the weather forecasts must have high spatial and temporal resolution which is generally not available. Also, the functional relationship between solar PV power and weather parameters is to be correctly determined. Considering these factors, the authors have developed the forecast models using only time series data of solar PV power generation.

1.2. Literature review

Several researchers have suggested forecast methodologies for short-term solar PV power generation forecast. However, sufficient literature regarding the same problem in very short-term forecast horizon is not available. Ref. [11] used AR and autoregressive with exogenous inputs (ARX) models to predict the hourly value of solar PV power. They found that AR model works better if the forecast horizon is upto two hours. However, if the forecast horizons are longer then numerical weather predictions (NWP) are more important. This work further supports the choice of authors to consider only solar PV power time series for forecasting. Ref. [12] used radial basis function (RBF) neural network for short-term solar PV power prediction using past values of sky cover, transmissivity, relative humidity and wind speed. This model was able to outperform AR model. Such a method is actually indirect solar PV power forecasting. A comparison of following forecast models-persistent, ARIMA, k Nearest Neighbors (kNN), ANN and ANN optimized by genetic algorithm (GA) was done by Ref. [13] for solar PV power forecast, in which they found that ANN optimized by GA could work better than other models.

Ref. [14] used SARIMA model for solar PV power time series forecast. The forecast accuracy was further increased by forecasting the residuals using support vector machine (SVM). In the proposed hybrid model, SARIMA model captured the linearity in the data and SVM model captured non-linearity in the residuals. ANN was used to forecast solar irradiation and temperature by Ref. [15]. The forecasted solar radiation and temperature were converted to an equivalent solar PV power using another neural network. Ref. [16] used ARIMA, SVM, ANN and ANFIS for solar PV power generation

forecast. The forecasts of individual models were linearly combined after optimizing the combination parameters using GA. The hybrid model was found to perform better than individual models. Another hybrid model strategy was used by Ref. [17] in which they used an ANN based smart reforecast model for solar PV power forecast. This model used the predictions from the baseline forecast models (physical deterministic model, ARMA model or kNN model) and the measured past values of inputs to improve the performance of the baseline models. Ensemble methods are also quite popular in forecasting. Ref. [18] used an ensemble of ANN and SVR for very short-term solar PV power forecast. They considered both solar PV power data as well as past weather data and found that the past weather data did not offer significant advantages. The univariate ensemble of neural networks performed better than all other models.

A mixed wavelet neural network was used by Ref. [19]. They used a combination of Morlet and Mexican hat wavelet functions as the activation function for hidden layer neurons of a feedforward ANN. This model performed better at forecasting solar irradiance than other forecasting techniques. Again a SARIMA model was used by Ref. [20] to forecast solar PV power data and the results were compared with persistence model. Ref. [21] employed ANN to forecast hour ahead solar PV power. They used gradient descent optimization to determine initial parameters of an ANN. Using these values as initial inputs a meta-heuristic optimization technique- Shuffled Frog Leap Algorithm was used to determine optimal values of parameters. Ref. [22] used k nearest neighbor artificial neural network model for very short-term solar irradiance forecasting. Wavelet transform, Particle Swarm Optimization (PSO) and SVM was used by Ref. [23] for short-term solar PV power forecasting. They considered solar PV power as well as NWP data. The PSO was used to tune the parameters of SVM. An improved SVR and enhanced empirical mode decomposition (EEMD) was employed by Ref. [24] for solar PV power forecasting. The proposed model worked better than other conventional forecasting models. In Ref. [25] short term forecast of net active power difference between renewable generations and load was done. The authors used SVM model whose parameters were optimized using Grid-GA searching.

1.3. Contribution

The literature suggests that if two or more forecast models are combined together then better forecasting performance can be achieved. The main contributions of this paper are as follows:

1. The effect of wavelet decomposition of solar PV power generation time series on its forecast accuracy is studied. This study is carried out for different weather conditions.
2. A combination strategy of forecast models is suggested for the solar PV power data having positive effects of wavelet decomposition. The combination parameter updates itself over time.
3. The conventional hybrid forecast models use some combination of outputs obtained from constituent models to get the required forecast. But the proposed forecast model applies the combination strategy on the decomposed series. This helps in achieving better forecasts as the combination occurs at more detailed level.
4. Various numerical accuracy measures have been calculated to validate the proposed forecast model.

1.4. Organization

The paper organization is as - Section 2 explains the theory of

forecast models, wavelet decomposition and accuracy measures used in the research paper. Feature selection algorithm as well as model combination method is also explained in the same section. Section 3 describes the forecast models development procedure and the interpretation of obtained results. The concluding remarks are given in section 4.

2. Brief theory of forecast models and accuracy measures

2.1. Persistence model

A smart persistence model is used as a benchmark for comparing other forecast models. The forecasted solar PV power is provided by Eq. (1) [26].

$$P(t + mh) = \frac{P(t)}{P_{cs}(t)} \times P_{cs}(t + mh) \quad (1)$$

Here,

$P(t)$ = actual solar PV power at time t

$P_{cs}(t)$ = expected clear sky solar PV power at time t

$m = 1, 2$ or 3 (depends on the time at which forecasted value is to be found out).

h = resolution of solar PV power data points

This model states that the ratio of actual solar PV power to the clear sky solar PV power remains constant between t and $t + mh$. The clear sky Global Horizontal Irradiance (GHI) is obtained using the information given in Ref. [27] and a linear relationship between GHI and power output is assumed as stated in Ref. [28].

2.2. Seasonal autoregressive integrated moving average (SARIMA)

SARIMA is one of the most widely used linear models for time series forecasting [29]. The general equation of this model is given by Eq. (2).

$$\phi(L)(1-L)^d\phi(L)(1-L^s)^Dy_t = c + \theta(L)\theta(L)e_t \quad (2)$$

Here y_t is time series, e_t is white noise and L is the lag operator. D represents the seasonal differentiation order and d represents regular differentiation order.

$$\phi(L) = 1 - \phi_1L - \phi_2L^2 - \dots \dots \phi_pL^p \quad (3)$$

$$\theta(L) = 1 + \theta_1L + \theta_2L^2 + \dots \dots \theta_qL^q \quad (4)$$

Eq. (3) and Eq. (4) represent the autoregressive and moving average polynomial respectively. They represent the dependence of future values of time series on past values as well as errors.

$$\phi(L) = 1 - \phi_{p1}L - \phi_{p2}L^{p2} - \dots \dots \phi_{pP}L^P \quad (5)$$

$$\theta(L) = 1 + \theta_{q1}L + \theta_{q2}L^{q2} + \dots \dots \theta_{qQ}L^Q \quad (6)$$

Similarly Eq. (5) and Eq. (6) represent the seasonal autoregressive and seasonal moving average polynomial respectively. Addition of these polynomials to the ARIMA equation helps in capturing the seasonal variation in time series. Differentiation is necessary for converting the non-stationary time series to a stationary one. s represents the order of seasonality which can be found out by Fast Fourier Transform (FFT) plot.

2.3. Wavelet transform

Fourier transform has always been a popular tool to determine the frequency components present in a particular signal. However, it suffers from one limitation that it does not provide any information regarding the time duration for which a particular frequency component is present in the signal. To overcome this limitation Short Time Fourier Transform (STFT) as given in Eq. (7) is used which basically calculates the Fourier transform over a narrow window of the signal.

$$STFT(t', f) = \int_t x(t)f(t - t')e^{-j\omega t} dt \quad (7)$$

Here $x(t)$ is the signal whose STFT is to be calculated and $f(t)$ is the window function. However, in accordance with the Heisenberg uncertainty principle it is not possible to exactly determine which frequency component is present at what time. The STFT can only give the details about the bands of frequencies that are present in a signal for some particular duration of time. Therefore if the window function is made narrower to obtain a good time resolution then the frequency resolution will become poorer and vice versa. Thus while applying STFT, there will always be a compromise between time and frequency resolutions.

The wavelet transform [30] can solve this problem of STFT to some extent. Eq. (8) represents the calculation of continuous wavelet transform (CWT).

$$CWT(b, a) = \frac{1}{\sqrt{|a|}} \int x(t)\psi\left(\frac{t-b}{a}\right) dt \quad (8)$$

Here $x(t)$ is the signal whose wavelet transform is to be calculated and $\psi(t)$ is the mother wavelet. a and b are called the dilation (or scale) and translation parameter respectively. To calculate CWT, the mother wavelet is dilated by using some suitable value of a and then translated over the entire signal. The same procedure is repeated for other values of dilation parameter. Most of the real world signals have high-frequency components for short duration of time and low-frequency components exist throughout the signal. The wavelet transform is formulated in a such a way that it is able to get good time resolution and poor frequency resolution at low scale and poor time resolution and good frequency resolution at high scale. Thus it helps in better representation of such signals.

As the computers are able to calculate CWT only at a finite number of points Eq. (9) gives the discretized version of CWT.

$$\bar{x}_{k,m} = \int_{-\infty}^{\infty} x[t] \frac{1}{\sqrt{2^k}} \psi\left(\frac{t - m2^k}{2^k}\right) dt \quad (9)$$

Here 2^k is the scale parameter and $m2^k$ is the translation parameter. Reconstruction of the original signal can be obtained by Eq. (10)

$$x[t] = \sum_k \sum_m \bar{x}_{k,m} 2^{-\frac{k}{2}} \psi\left(\frac{t - m2^k}{2^k}\right) \quad (10)$$

Another version of wavelet transform - Discrete Wavelet Transform (DWT) is preferred over CWT as the computers are able to calculate only the discretized version of CWT which consumes large time. On the other hand, DWT provides sufficient information about the signal in lesser time. The DWT uses the pyramid algorithm which requires decomposition high pass and low pass filters to separate the bands of frequencies present in the signal. The algorithm is given as:

1. To obtain the first level of approximation and detailed series, the original series is passed through low pass and high pass filters to give approximation series - a1 and detailed series - d1 respectively (Fig. 1).
2. Both of the series so obtained are downsampled by two.
3. The series - a1 obtained in the previous step is passed through high pass as well as low pass filters to obtain the approximation and detailed series at second level denoted by - a2 and d2.
4. The series - a2 and d2 are downsampled by two and the same procedure is repeated again. Fig. 1 shows three level decomposition of the series. The finally obtained approximation series is a3 and detailed series are d1, d2 and d3.

Using the reconstruction filters, the original series can be written as a sum of approximation and detailed series given by Eq. (11).

$$x[t] = A + \sum_{l=1}^L D_l \quad (11)$$

Here

A is approximation series, D's are various detailed series and L is the level of decomposition.

The authors have used maximum overlap discrete wavelet transform (MODWT) [31]. Its key advantages over regular DWT are:

- (1) The MODWT is a highly redundant and non-orthogonal transform. This redundancy helps in the alignment of original time series with the series of decomposed coefficients. This property is particularly important in forecasting applications.
- (2) In DWT, for a decomposition at J levels, the length of series N must be a multiple of 2^J . However, MODWT is defined for the series of all lengths. This property is also necessary for forecasting as the length of the encountered series may not always be a multiple of 2^J .

2.4. Time based a trous filter algorithm

As a rolling window forecast is needed to be carried out, therefore the solar PV power data is also needed to be decomposed in a rolling window manner. The time based a trous filter algorithm [32] can produce an appropriate representation of the data. The procedure is given as follows

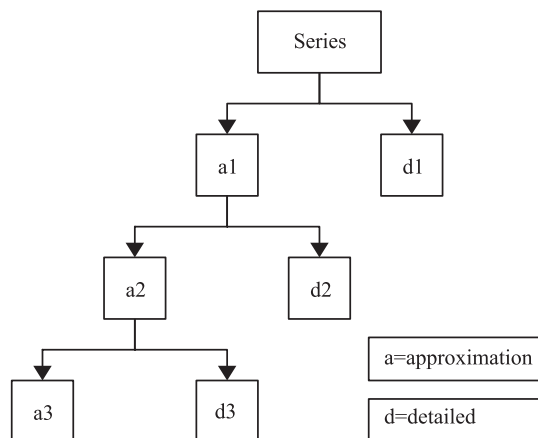


Fig. 1. Pyramid algorithm.

- (1) Consider a section of time series starting from value $x(1)$ upto $x(n)$, i.e. $x(1), x(2), \dots, x(n)$.
- (2) This section is decomposed into sub-series using MODWT. Only the last elements of the decomposed sub-series are retained and the rest are discarded.
- (3) A new section is formed by including the next value in the time series with the original section- $x(1), \dots, x(n), x(n+1)$.
- (4) This section is again decomposed using MODWT and only the last values in each sub-series are retained.
- (5) All the above steps are repeated for whole solar PV power data. Fig. 2 explains the whole procedure.

2.5. Random vector functional link (RVFL) neural network

The neural networks have become quite popular for determining the functional relationship between the input and output variables of a system. They are generally trained using error back-propagation method. But this method suffers from some disadvantages like the update algorithm may get stuck in local minima and the final solution depends on the learning rate.

The Random Vector Functional Link (RVFL) [33] neural network overcomes these disadvantages. It can be structurally divided into three parts as shown in Fig. 3 - input layer, enhancement nodes and output layer. The weights from the input layer to the enhancement nodes are randomly chosen. Some suitable activation function can be used for enhancement nodes. Only the weights from the enhancement nodes to the output layer are needed to be determined. This neural network has direct linkages from the input layer to output layer which further helps in mapping relationship between inputs and outputs. There are two methods to determine the weights between enhancement nodes and output layer:

1. Moore-Penrose pseudoinverse.
2. L2 norm regularized least squares (ridge regression).

2.6. Maximum relevance minimum redundancy (MRMR) algorithm

This algorithm has been used by the authors for feature selection. The maximum relevance minimum redundancy algorithm [34] selects those features that have strong relationship with the target and at the same time weak relationship among themselves. It achieves this using mutual information criteria as given by Eq. (12).

$$I(a, b) = \sum_{ij} p(a_i, b_j) \log \frac{p(a_i, b_j)}{p(a_i)p(b_j)} \quad (12)$$

Here $p(a_i)$ and $p(b_j)$ are the marginal probabilities of discrete variables a_i and b_j . $p(a_i, b_j)$ is the joint probability distribution for these variables.

Let x be the feature set, t be the target and S denotes selected feature set. To select features with maximum relevance Eq. (13) is needed to be maximized.

$$\max U_i, \quad U_i = \frac{1}{|S|} \sum_{i \in S} I(x_i, t) \quad (13)$$

At the same time the features having minimum redundancy among them should be selected. This is represented by Eq. (14).

$$\min V_i, \quad V_i = \frac{1}{(|S|)^2} \sum_{ij \in S} I(x_i, x_j) \quad (14)$$

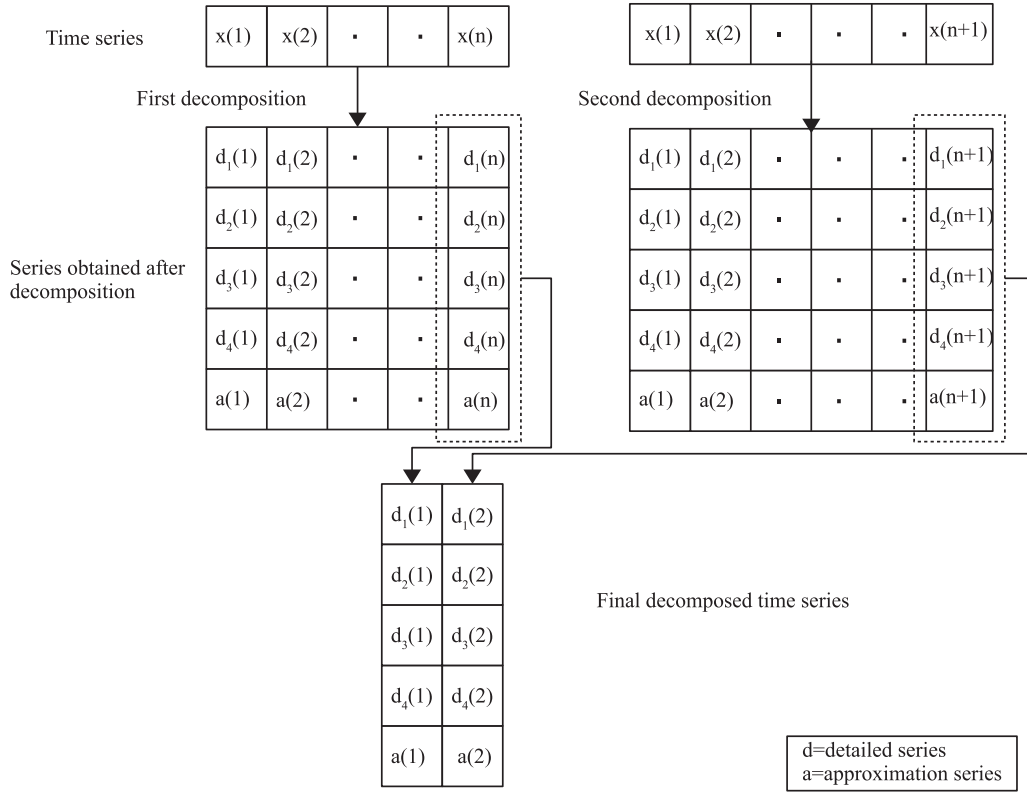


Fig. 2. Time based a trous filter algorithm.

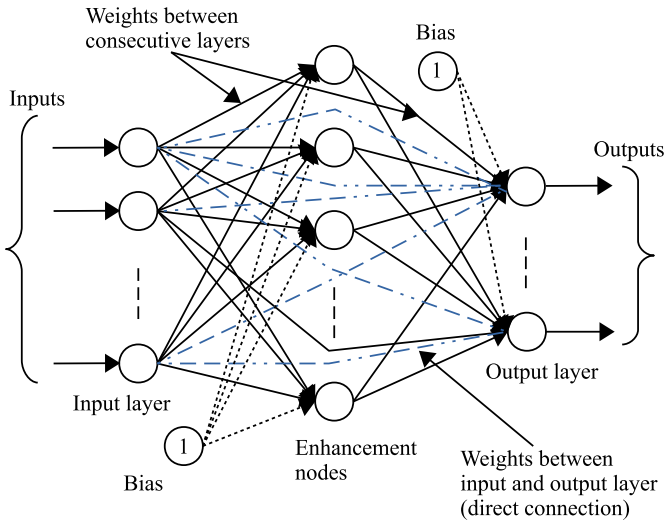


Fig. 3. Block diagram of Random Vector Functional Link neural network.

These two can be combined in one maximization equation. Suppose we have already obtained S_{n-1} feature set with $(n-1)$ features. The next step will be to select the n th feature from set $X - S_{n-1}$. This is actually the maximization of Eq.(15).

$$x_i \in X - S_{n-1} \left[I(x_i, t) - \frac{1}{n-1} \sum_{x_j \in S_{n-1}} I(x_i, x_j) \right] \quad (15)$$

2.7. Convex combination of adaptive filters

The convex combination of adaptive filters is used in signal processing to get the best performance out of two filters [35] having slightly different characteristics. As shown in Fig. 4, a common input signal is applied to both filters. Let the output of two filters be given as y_1 and y_2 . The final output y is a linear combination of the two outputs and is given by Eq. (16).

$$y(n) = \lambda(n)y_1(n) + (1 - \lambda(n))y_2(n) \quad (16)$$

The combined output is compared with the desired signal to obtain the error. This error can be used to adjust the multiplying factor (λ) and filter coefficients so that the actual output obtained matches the desired signal. While updating λ , it may happen that the value of λ becomes greater than one. To avoid such a situation λ is equated to a function of α given by Eq. (17)

$$\lambda(n) = \frac{1}{1 + e^{-\alpha(n)}} \quad (17)$$

The update equation of α is given as

$$\begin{aligned} \alpha(n+1) &= \alpha(n) - \frac{\mu}{2} \frac{\partial e^2}{\partial \alpha(n)} \\ &= \alpha(n) - \frac{\mu}{2} \frac{\partial e^2(n)}{\partial \lambda(n)} \frac{\partial \lambda(n)}{\partial \alpha(n)} \\ &= \alpha(n) + \mu e(n)[y_1(n) - y_2(n)]\lambda(n)[1 - \lambda(n)] \end{aligned} \quad (18)$$

This combination strategy of signal filters can also be used to combine forecast models so as to get better performance than individual ones. The research paper has considered only the update of combination parameter and no change in forecast models with time.

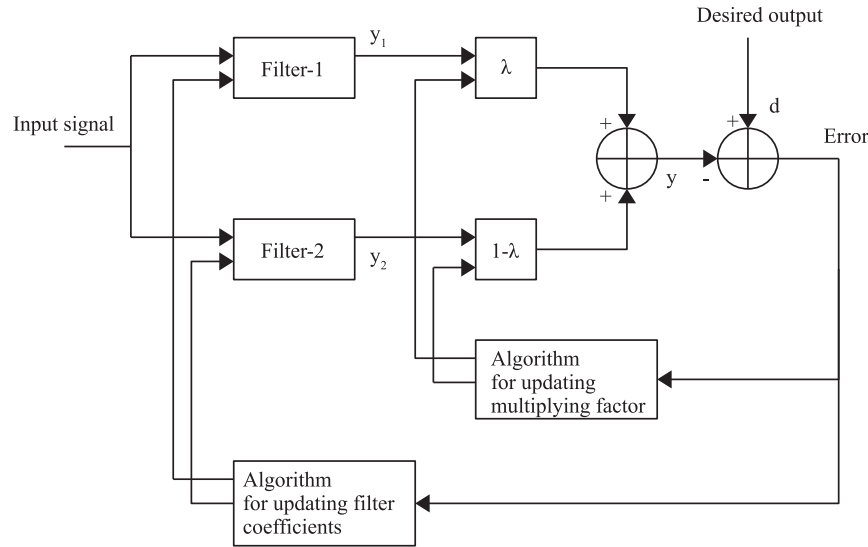


Fig. 4. Block diagram of convex combination of filters.

2.8. Forecast accuracy measures

Four forecast accuracy measures have been used for assessing the forecast accuracy which are given by Eq. (19)–(23).

Mean Absolute Percentage Error (Eq. (19))

$$MAPE = \frac{1}{N} \sum_{i=1}^N \frac{|P_{actual}(i) - P_{forecast}(i)|}{P_{average}} \times 100\% \quad (19)$$

where

$$P_{average} = \frac{1}{N} \sum_{i=1}^N P_{actual}(i) \quad (20)$$

Root mean square error (Eq. (21))

$$RMSE = \sqrt{\frac{\sum_{i=1}^N (P_{actual}(i) - P_{forecast}(i))^2}{N}} \quad (21)$$

Mean absolute scaled error (Eq. (22))

$$MASE = \frac{\frac{1}{N} \sum_{i=1}^N |P_{actual}(i) - P_{forecast}(i)|}{\frac{1}{N-m} \sum_{i=m+1}^N |P_{actual}(i) - P_{actual}(i-m)|} \quad (22)$$

Coefficient of determination (Eq. (23))

$$R^2 = 1 - \frac{\sum_{i=1}^N (P_{actual}(i) - P_{forecast}(i))^2}{\sum_{i=1}^N (P_{actual}(i) - P_{average})^2} \quad (23)$$

3. Forecast model development - A case study at IIT Gandhinagar campus

The total installed capacity of solar PV systems at IIT Gandhinagar campus is 500 kWp. This can be divided into three parts which includes installations at academic blocks, student hostels and solar carport. The total installed capacity at academic blocks is 191.8 kWp and at student hostels it is 120 kWp. Further details of solar PV systems at these sites is given in Table 1. The 25 kWp

Table 1

Details of solar PV installations at IIT Gandhinagar.

Name of academic block	Installed capacity (kWp)	Name of hostel	Installed capacity (kWp)
AB-1	25	Aibaan	25
AB-2	25	Beauki	15
AB-3	22.75	Chimair	15
AB-4	89.05	Duven	15
AB-5	15	Emiet	25
AB-6	15	Firpeal	25

installations consist of a total of 85 modules in 5 strings and 15 kWp installations consist of a total of 51 modules in 3 strings. The installed capacity of Solar Carport is 192.8 kWp. Fig. 5 shows some of the solar PV sites at IIT Gandhinagar.

The resolution of the solar PV power data obtained from inverters is 20 min. The corresponding data of 15 kW inverter installed at Beauki hostel is used for the forecast model development purpose. This data is divided into two parts according to the weather conditions:

- **Clear sky data** - It consists of solar PV power data of April 2017 and May 2017 month. The data of April 2017 is used for model development and that of May 2017 for testing purpose.
- **Cloudy/Rainy weather data** - It consists of solar PV power data of June 2017 and July 2017 month. On the same line as that of clear sky data, June 2017 month's data is used for model development and that of July 2017 for testing purpose.

The forecasting is done for the first ten days of testing month for both the data. The different forecast horizons considered are one step ahead, two steps ahead and three steps ahead. Here, a single step refers to a time duration of 20 min. While doing a two steps ahead forecast, the input data to a forecast model will consist of one forecasted value and the actual values prior to that forecasted value. Similar concept can be extended to three steps ahead forecasting as well.

3.1. Forecast models for solar PV power generation in clear sky weather

For the present case study two forecast models - SARIMA and



Fig. 5. Solar PV sites at IIT Gandhinagar campus.

RVFL neural network have been used. The normal as well as wavelet decomposed time series have been evaluated as inputs.

3.1.1. SARIMA

Fig. 6 shows the autocorrelation function (ACF) and partial autocorrelation function (PACF) plots of solar PV power generation data which suggest a daily seasonality of 72 data points (the same number of data points as in a day). For the SARIMA model development different candidate models were considered. The

maximum number of AR and MA lags was kept five after analyzing the ACF and PACF plots. Among different candidate models, the one with minimum Bayesian Information Criterion (BIC) was selected for the forecasting task. $ARIMA(5,1,2) \times (0,1,1)_{72}$ was found suitable for our data.

3.1.2. Wavelet SARIMA (W-SARIMA)

To develop this model, the original time series was decomposed into five sub-series using MODWT and time based a trous filter

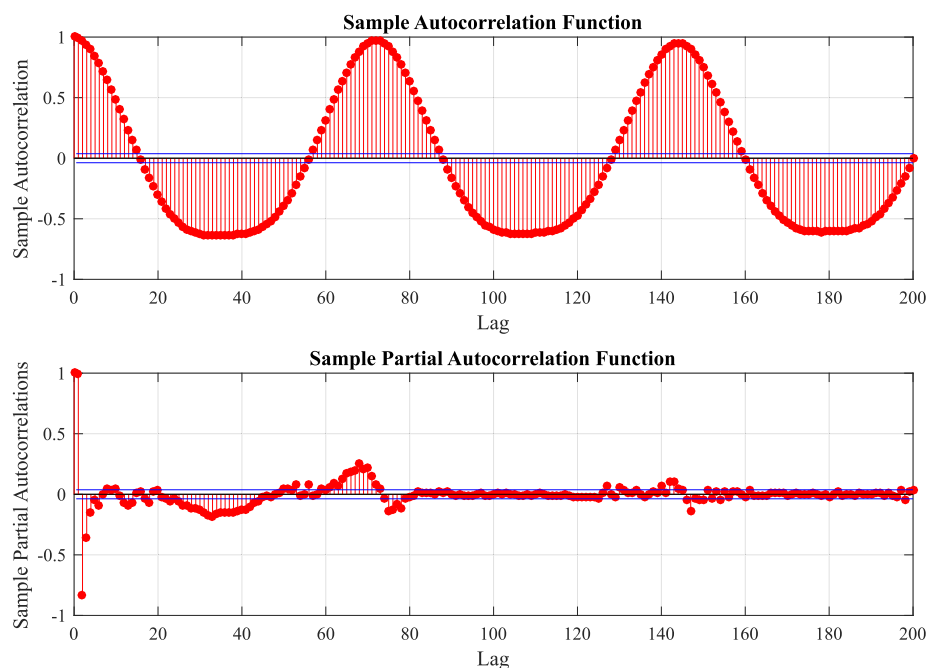


Fig. 6. ACF and PACF plots of the solar PV power generation data.

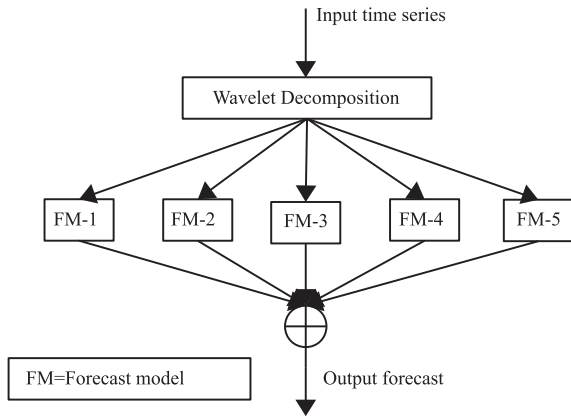


Fig. 7. Block diagram of W-SARIMA/W-RVFL model.

algorithm in a rolling window manner. The decomposed series are shown in Fig. 8. Here, A is the approximate low frequency series and D4, D3, D2 and D1 are the high frequency series. So obtained series were forecasted using separate forecast models. Each of the individual forecasts so obtained was summed up to give the value of actual forecast. Fig. 7 describes the same procedure in block diagram form. Here forecast model can be replaced by ARIMA/SARIMA. The ARIMA/SARIMA forecast models chosen for all the decomposed series using the previously described method is given in Table 2.

Table 2
Forecast models for decomposed series of clear sky data.

S.No.	Decomposed series	ARIMA/SARIMA forecast model
1	A	ARIMA(5,1,5) \times (1,1,1) ₇₂
2	D4	ARIMA(4,1,5) \times (1,1,1) ₇₂
3	D3	ARIMA(3,1,4) \times (1,1,1) ₇₂
4	D2	ARIMA(3,1,3) \times (1,1,1) ₇₂
5	D1	ARIMA(1,1,5) \times (1,1,1) ₇₂

3.1.3. RVFL

A random vector functional link neural network with eighteen number of enhancement nodes and radial basis activation function was found suitable for the current task. The best ten past values to be used as inputs were selected using MRMR algorithm as described in section 2.6. So obtained past values were

$$P_{t-1}, P_{t-2}, P_{t-3}, P_{t-70}, P_{t-71}, P_{t-72}, P_{t-73}, P_{t-74}, P_{t-143}, P_{t-144}$$

The weights between input layer and enhancement layer were randomly selected from uniform distribution and Moore Penrose pseudoinverse was used to determine the values of weights between enhancement layer and output layer.

3.1.4. Wavelet RVFL (W-RVFL)

The wavelet RVFL model is identical to wavelet SARIMA model except that in place of SARIMA model, RVFL neural network model is used (Fig. 7). The best ten features for individual series were selected using MRMR algorithm and separate RVFL models were employed to carry out the forecasting. The best ten past lags were

$$P_{t-1}, P_{t-2}, P_{t-70}, P_{t-71}, P_{t-72}, P_{t-73}, P_{t-74}, P_{t-142}, P_{t-143}, P_{t-144}$$

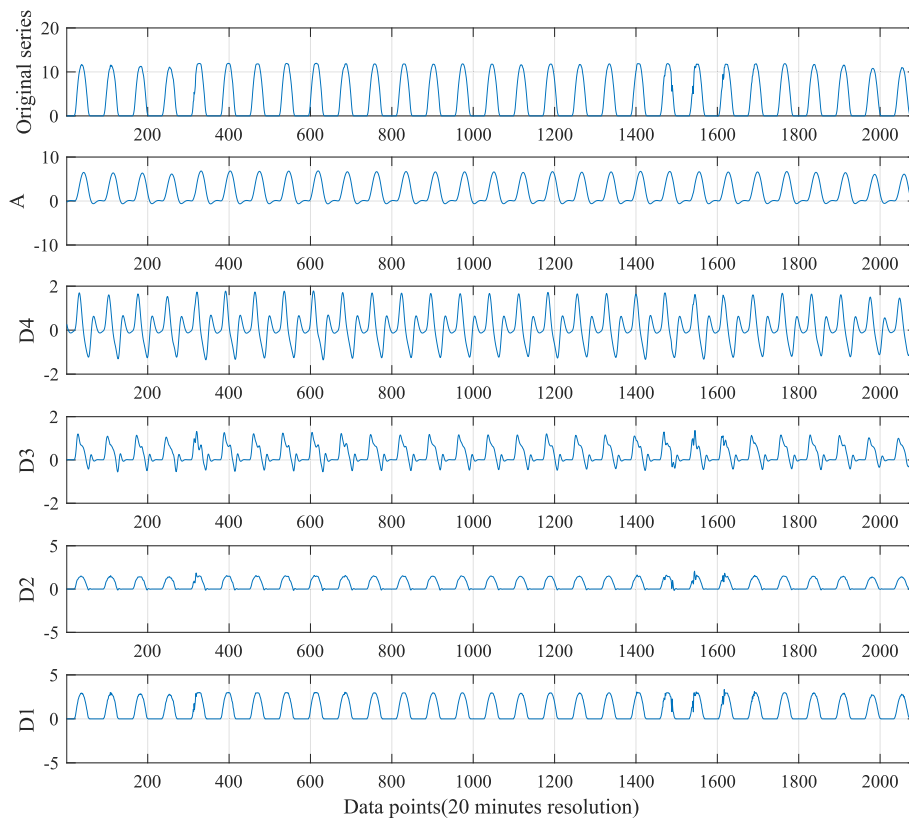


Fig. 8. Wavelet decomposition of solar PV power time series.

These lags were found common for all the series. Each of the so obtained forecast was summed up to obtain the actual forecast. Table 3 shows the number of neurons in enhancement layer for the forecast models of different series. These were obtained by testing the performance of RVFL neural networks with different number of neurons in enhancement layer for a small section of data. Again radial basis activation function was used in the enhancement layer and determination of weights between output and enhancement layer was done using pseudoinverse. The radial basis activation function are quite popular in literature and the performance of this activation function was found better as compared to other activation functions.

3.1.5. Result comparison of developed models

Table 4 shows the values of forecast accuracy measures for all the above developed models. There is an increase in values of errors as well as error variance as the forecast horizon increases. The value of coefficient of determination does not change much with an increase in forecast horizon.

The performance of SARIMA model is found to be slightly better than all the other forecast models. The value of error variance is also less for this model.

The W-SARIMA model has higher values of errors as compared to the SARIMA model. Eq. (24) has been used to compare the MAPE of these two models.

$$\delta_{MAPE} = \frac{MAPE_{W-SARIMA} - MAPE_{SARIMA}}{MAPE_{SARIMA}} \times 100\% \quad (24)$$

The MAPE of W-SARIMA model for the three forecast horizons (increasing order) is 26.1%, 36.3% and 43% higher as compared to SARIMA model. One possible reason for this could be that as the sky is clear there is no high-frequency component in solar PV power data and thus no advantage is associated with series decomposition. The decomposition, forecasting and subsequent reconstruction complicates the model development process and thus it becomes prone to ill-fitting. For RVFL and W-RVFL models one step

ahead forecast MAPE is almost comparable. However, the errors associated with W-RVFL model start to increase as compared with RVFL model as the forecast horizon increases.

Percent change in the values of accuracy measures of a model, as the forecast horizon increases (Eq. (25)) can also be used to compare them.

$$\delta_{AM} = \frac{AM_{two/three} - AM_{one}}{AM_{one}} \times 100\% \quad (25)$$

where AM_{one} = one step ahead accuracy measure

and $AM_{two/three}$ = two/three steps ahead accuracy measure

Table 5 shows the values of Eq. (25) obtained for different forecast models. It can be seen that for RVFL model the percent change in forecasting error is less as compared to other models as the forecast horizon increases.

The actual and forecasted solar PV power time series for all the models and for one time step ahead forecast is shown in Fig. 9 and the daywise variation of MAPE and RMSE is shown in Fig. 10 for the same forecast horizon. The day, 5th May 2017 was little cloudy and the values of errors associated with wavelet assisted models is high as the models have not been trained for such an intermittent data. All these observations suggest that for the case of clear sky data the wavelet decomposition is not aiding the forecast models to improve accuracy.

3.2. Forecast models for solar PV power generation in cloudy/rainy weather

All the four forecast models that were developed earlier, were also developed for the cloudy/rainy weather data using same procedure. In addition, a support vector regression (SVR) model has been also developed. Table 6 shows the order of ARIMA/SARIMA models chosen for the decomposed series. ARIMA models were chosen for series D2 and D1 instead of SARIMA models. This is so because random variations are prominent in these series. Thus only a little periodicity is present in them.

The number of neurons selected for Wavelet RVFL models is given in Table 7 and the input past lags for these models is given in Table 8.

3.2.1. SARIMA-RVFL hybrid model

Table 9 shows the comparison of performances of different forecast models. The SARIMA-RVFL hybrid model shows some improvement over other models. This improvement in performance can be attributed to the fact that local high-frequency variations in the solar PV power data introduced due to clouds were separated using wavelet decomposition and forecasted using different forecast models.

The authors suggest simultaneous use of two wavelet assisted forecast models to give better accuracy than individual ones. Fig. 11 shows the block diagram of proposed forecast strategy. The original solar PV power time series was decomposed into five sub-series. For each of the sub-series, two forecast models - SARIMA and RVFL neural network were used. This gave two values of forecast. These two values were linearly combined using the convex combination method as discussed in section 2.7 to get a better forecast. This procedure was followed for each of the five sub-series. The required forecast was obtained after summing up the five forecasts. In this method, the parameter lambda updates its value with time and thus the model performs well even if the series behaviour changes a little.

Table 3
Number of neurons in enhancement layer for decomposed series of clear sky data.

S.No.	Decomposed series	Number of neurons in enhancement layer
1	A	21
2	D4	13
3	D3	96
4	D2	42
5	D1	51

Table 4
Comparison of forecast models for May month.

S.No.	Forecast model	Steps	MAPE	RMSE	MASE	R ²	Error variance
1	Persistence	One	3.613	0.322	0.804	0.994	0.103
		Two	4.758	0.395	1.058	0.991	0.153
		Three	5.072	0.401	1.128	0.990	0.159
2	SARIMA	One	2.723	0.281	0.605	0.995	0.079
		Two	3.010	0.306	0.669	0.994	0.094
		Three	3.100	0.299	0.689	0.994	0.089
3	W-SARIMA	One	3.434	0.353	0.763	0.992	0.125
		Two	4.103	0.414	0.912	0.990	0.172
		Three	4.436	0.421	0.986	0.989	0.178
4	RVFL	One	3.050	0.287	0.678	0.995	0.082
		Two	3.247	0.290	0.722	0.995	0.083
		Three	3.323	0.292	0.738	0.995	0.084
5	W-RVFL	One	3.007	0.290	0.668	0.995	0.084
		Two	3.262	0.300	0.725	0.994	0.090
		Three	3.578	0.335	0.795	0.993	0.112

Table 5
Comparison of percent changes in accuracy measures for May month.

S.No.	Forecast Model	Steps	Percent change				
			Δ MAPE	Δ RMSE	Δ MASE	ΔR^2	Error variance
1	Persistence	Two	31.691	22.671	31.592	−0.302	48.544
		Three	40.382	24.534	40.299	−0.402	54.369
2	SARIMA	Two	10.539	8.896	10.578	−0.100	18.987
		Three	13.845	6.405	13.884	−0.100	12.658
3	W-SARIMA	Two	19.481	17.280	19.528	−0.201	37.600
		Three	29.178	19.263	29.226	−0.302	42.400
4	RVFL	Two	6.459	1.045	6.489	0	1.219
		Three	8.950	1.742	8.849	0	2.439
5	W-RVFL	Two	8.480	3.448	8.532	−0.100	7.142
		Three	18.989	15.517	19.012	−0.201	33.333

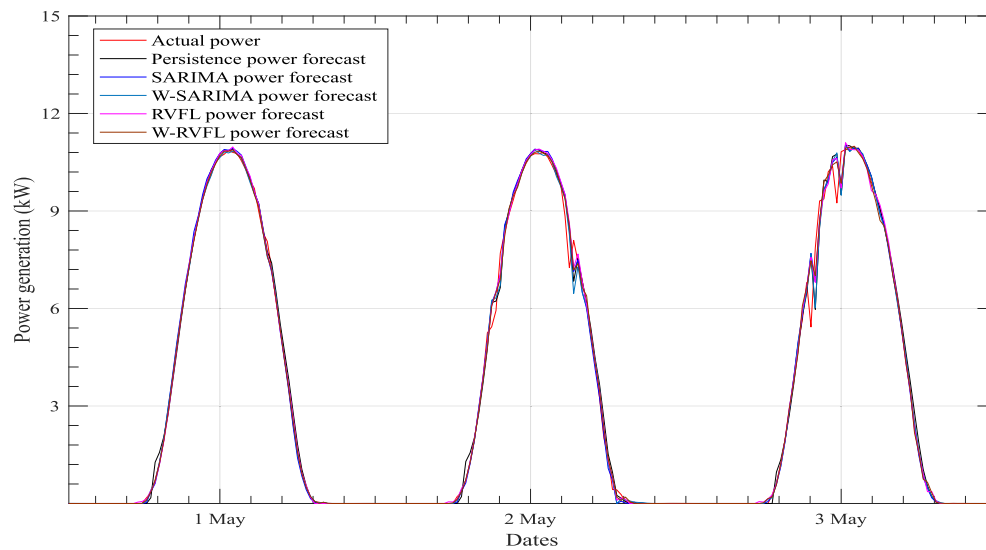


Fig. 9. Actual and forecasted solar PV power in May month for one step ahead forecast horizon.

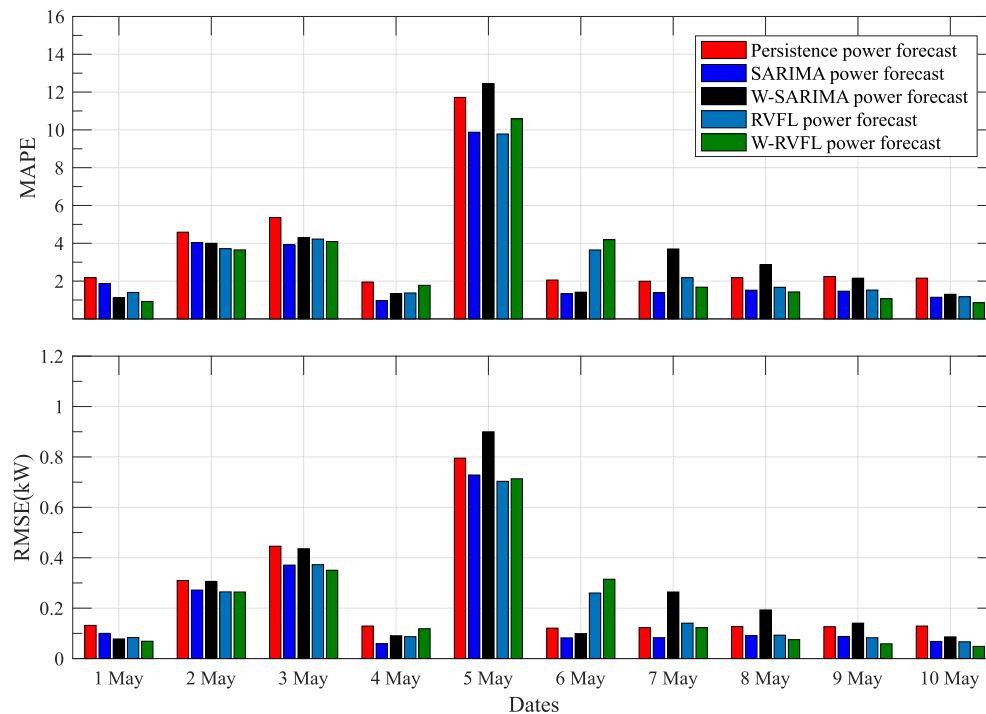


Fig. 10. MAPE and RMSE of all models for different days in May month for one step ahead forecast horizon.

Table 6
Forecast models for decomposed series of cloudy/rainy sky data.

S.No.	Decomposed series	ARIMA/SARIMA forecast model
1	A	ARIMA(5,0,5)×(0,1,1) ₇₂
2	D4	ARIMA(5,0,1)×(1,1,1) ₇₂
3	D3	ARIMA(5,0,3)×(1,1,1) ₇₂
4	D2	ARIMA(5,0,5)
5	D1	ARIMA(2,0,5)

Table 7
Number of neurons in enhancement layer for decomposed series of cloudy/rainy sky data.

S.No.	Decomposed series	Number of neurons in enhancement layer
1	A	26
2	D4	35
3	D3	42
4	D2	17
5	D1	82

Table 8
Selected features for forecast models of decomposed series of cloudy/rainy sky data.

S.No.	Decomposed series	Past Lags
1	A	$P_{t-1}, P_{t-2}, P_{t-3}, P_{t-70}, P_{t-71},$ $P_{t-72}, P_{t-73}, P_{t-74}, P_{t-143}, P_{t-144}$
2	D4	$P_{t-1}, P_{t-2}, P_{t-3}, P_{t-70}, P_{t-71},$ $P_{t-72}, P_{t-73}, P_{t-74}, P_{t-143}, P_{t-144}$
3	D3	$P_{t-1}, P_{t-2}, P_{t-69}, P_{t-70}, P_{t-71},$ $P_{t-72}, P_{t-73}, P_{t-74}, P_{t-143}, P_{t-144}$
4	D2	$P_{t-1}, P_{t-68}, P_{t-70}, P_{t-71}, P_{t-72},$ $P_{t-73}, P_{t-74}, P_{t-75}, P_{t-143}, P_{t-144}$
5	D1	$P_{t-1}, P_{t-2}, P_{t-3}, P_{t-70}, P_{t-71},$ $P_{t-72}, P_{t-73}, P_{t-74}, P_{t-143}, P_{t-144}$

Table 9
Comparison of forecast models for July month.

S.No.	Forecast model	Steps	MAPE	RMSE	MASE	R ²	Error variance
1	Persistence	One	20.876	1.021	0.623	0.906	1.043
		Two	22.792	1.052	0.680	0.900	1.109
		Three	24.470	1.123	0.730	0.866	1.262
2	SARIMA	One	25.395	1.091	0.757	0.892	1.191
		Two	28.276	1.182	0.843	0.873	1.398
		Three	30.860	1.284	0.920	0.851	1.651
3	W-SARIMA	One	21.146	0.969	0.630	0.915	0.940
		Two	23.105	1.012	0.689	0.907	1.024
		Three	25.803	1.117	0.769	0.887	1.248
4	RVFL	One	22.233	1.006	0.663	0.908	1.005
		Two	24.469	1.103	0.729	0.890	1.205
		Three	27.195	1.243	0.811	0.860	1.538
5	W-RVFL	One	20.839	0.952	0.621	0.918	0.906
		Two	21.984	0.992	0.655	0.911	0.984
		Three	24.603	1.103	0.733	0.890	1.218
6	SVR	One	22.503	1.032	0.671	0.904	1.058
		Two	24.489	1.126	0.731	0.885	1.253
		Three	26.529	1.211	0.791	0.867	1.448
7	Proposed	One	19.762	0.915	0.589	0.924	0.837
		Two	21.022	0.947	0.627	0.918	0.897
		Three	23.846	1.054	0.711	0.899	1.111

3.2.2. Result comparison of developed models

Table 9 shows that proposed model outperforms other forecast models. The value of error variance of the proposed forecast model is less and that of coefficient of determination is high as compared to other forecast models. This is due to the fact that the convex combination of forecast models promotes the forecasted value of that model which has performed better in the past. Also the proposed model combines forecasts of decomposed series which is equivalent to combining the forecast models at more detailed level. Using Eq.(25), percentage change in accuracy measures as the forecast horizon increases has been calculated and given in Table 10 for comparison purposes.

The percentage improvement in performance of proposed forecast model as compared to other models can be calculated using Eq. (26) and is given in Table 11.

$$\delta_{AM} = \frac{AM_{model} - AM_{proposed}}{AM_{model}} \times 100\% \quad (26)$$

where

AM_{model} = accuracy measures of conventional forecast models
 $AM_{proposed}$ = accuracy measures of proposed forecast model

It can be seen from Table 11 that there is considerable improvement in error measures as well as error variance on comparison with all the other forecast models. The actual and forecasted solar PV power time series for July month (one step ahead forecast) is given in Fig. 12. The first three days are rainy and thus power generation is very low and at the same time highly intermittent. Rest of the days are classified as cloudy.

To get a more detailed view of the forecasts produced by various models, Fig. 13 shows forecasted time series on 2nd July 2017. The error histogram of forecast errors (one step ahead forecast) for all the five models is shown in Fig. 14. The errors are expressed as a percentage of installed capacity which is 15 kW.

To get a further detailed view an arbitrary rainy day 1st July 2017 has been chosen. The MAPE and RMSE values on the same day for all the forecast models is shown in Fig. 15. The proposed model has performed better for all the three forecast horizons.

Fig. 16 shows the values of accuracy measures associated with the decomposed series on 1st July 2017. This gives an insight into the working of hybrid model. It is observed that all the forecast models have comparable accuracy while forecasting smooth series but it gets reduced with an increase in high frequency content. In such situations the combination of forecast models is able to perform well.

4. Conclusion

This research paper has presented the well known concept of wavelet and its application in forecasting. It is observed that in clear sky conditions, the wavelet decomposition tends to reduce the forecast accuracy. This happens due to increased complexity in forecast model development which is not compensated by advantages offered due to data decomposition. Only a single forecast model like SARIMA or RVFL is sufficient in such a case. However in the cloudy/rainy sky conditions, when high-frequency variations are present in the solar PV power then wavelet decomposition will aid the forecast model to perform better. The proposed SARIMA-RVFL hybrid model employs the same concept and has been found to show better results than its constituent models. But switching between two forecast models is a difficult task and thus requires implementation of other algorithms. The future work may involve development of simple algorithms for switching between

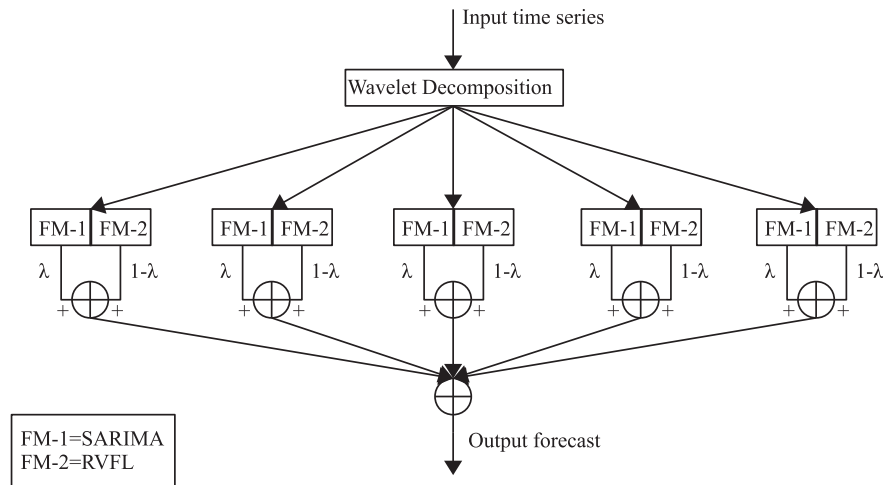


Fig. 11. Block diagram of proposed model.

Table 10

Comparison of percent changes in accuracy measures as the forecast horizon increases for July month.

S.No.	Forecast Model	Steps	Percent change				
			Δ MAPE	Δ RMSE	Δ MASE	ΔR^2	Error variance
1	Persistence	Two	9.178	3.036	9.149	−0.662	6.328
		Three	17.216	9.990	17.175	−2.208	20.997
2	SARIMA	Two	11.345	8.341	11.361	−2.130	17.380
		Three	21.520	17.690	21.532	−4.956	38.623
3	W-SARIMA	Two	9.264	4.438	9.365	−0.874	8.936
		Three	22.023	15.273	22.063	−3.060	32.766
4	RVFL	Two	10.057	9.642	9.955	−1.982	19.900
		Three	22.318	23.559	22.323	−5.286	53.035
5	W-RVFL	Two	5.495	4.202	5.475	−0.763	8.609
		Three	18.062	15.861	18.035	−3.050	34.437
6	SVR	Two	8.826	9.109	8.942	−2.102	18.431
		Three	17.891	17.345	17.884	−4.093	36.862
7	Proposed	Two	6.376	3.497	6.452	−0.649	7.169
		Three	20.666	15.191	20.713	−2.076	32.376

Table 11

Percentage improvement in performance of proposed model.

S.No.	Forecast model	Steps	Percent improvement				
			Δ MAPE	Δ RMSE	Δ MASE	ΔR^2	Error variance
1	Persistence	One	5.336	10.382	5.546	−1.987	19.751
		Two	7.766	9.981	7.794	−2.000	19.116
		Three	2.550	6.144	2.603	−1.467	11.965
2	SARIMA	One	22.181	16.132	22.192	−3.587	29.722
		Two	25.654	19.881	25.622	−5.154	35.836
		Three	22.728	17.912	22.717	−5.640	32.707
3	W-SARIMA	One	6.545	5.572	6.507	−0.983	10.957
		Two	9.015	6.422	8.998	−1.212	12.402
		Three	7.584	5.640	7.542	−1.352	10.977
4	RVFL	One	11.114	9.045	11.161	−1.762	16.716
		Two	14.087	14.143	13.991	−3.146	25.560
		Three	12.314	15.205	12.330	−4.534	27.763
5	W-RVFL	One	5.168	3.886	5.153	−0.653	7.615
		Two	4.375	4.536	4.274	−0.768	8.841
		Three	3.076	4.442	3.001	−1.011	8.784
6	SVR	One	12.181	11.337	12.221	−2.212	20.889
		Two	14.157	15.897	14.227	−3.729	28.412
		Three	10.113	12.965	10.114	−3.691	23.273

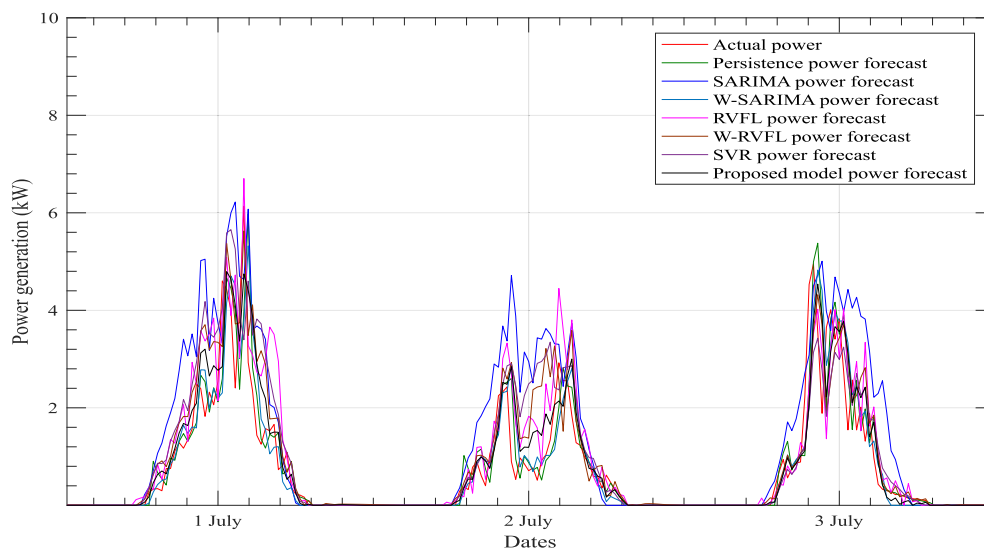


Fig. 12. Actual and forecasted solar PV power in July month.

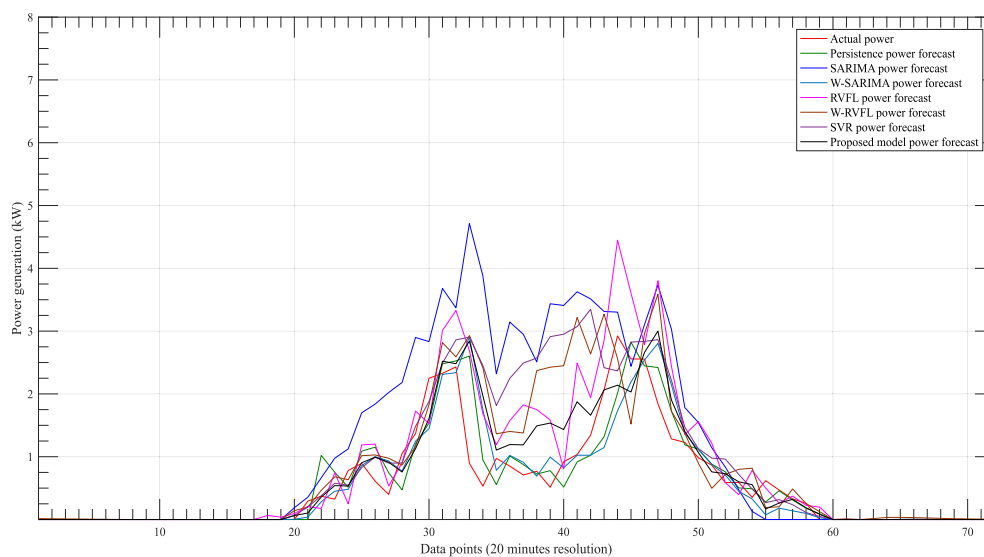


Fig. 13. Actual and forecasted solar PV power on 2nd July 2017.

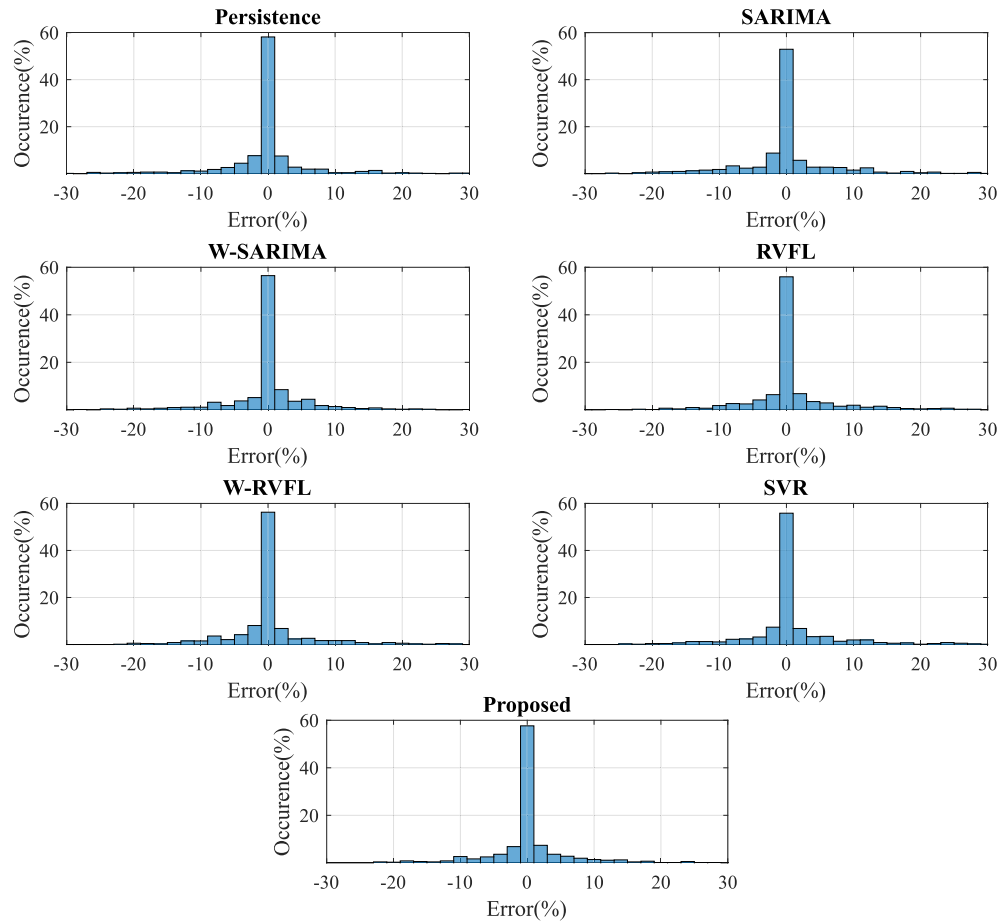


Fig. 14. Error histogram of all the forecast models.

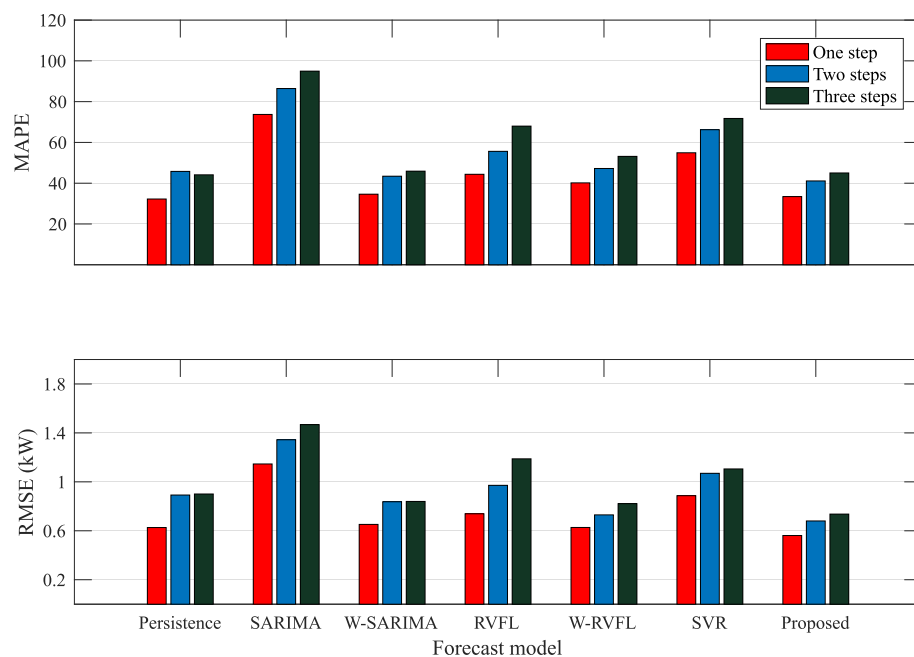


Fig. 15. Variation of MAPE and RMSE on 1st July 2017 as the forecast horizon increases.

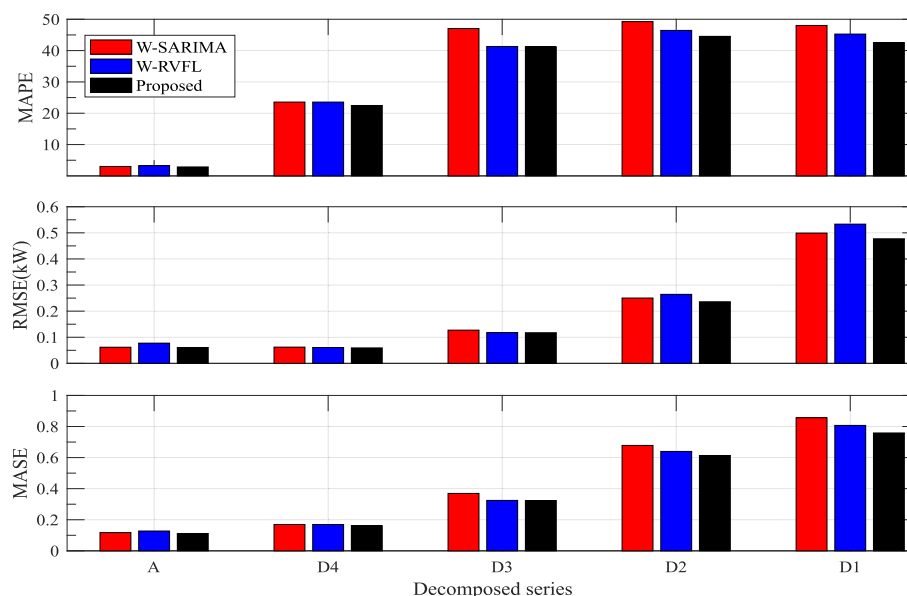


Fig. 16. Forecast accuracy measures of the five decomposed series on 1st July 2017 (one time step ahead).

forecast models and use of suitable weather parameters having good spatial and temporal resolution in the development of forecast models. Also, the feature selection algorithm can be made adaptive in nature.

Conflicts of interest

The authors declare no conflict of interest.

Acknowledgement

This work was supported by the Science and Engineering Research Board, a statutory body of Department of Science and Technology (DST), Government of India, under the grant no. EMR/2016/002037.

References

- [1] IEA, Trends 2017 in Photovoltaic Applications Executive Summary. http://www.iea-pvps.org/fileadmin/dam/public/report/statistics/IEA-PVPS_-_Trends_in_PV_Applications_2017_-_EXECUTIVE_SUMMARY.pdf. (Accessed 5 April 2018).
- [2] REN21, Advancing the Global Renewable Energy Transition. http://www.ren21.net/wp-content/uploads/2017/06/GSR2017_Highlights_FINAL.pdf. (Accessed 5 April 2018).
- [3] C. Wan, J. Zhao, Y. Song, Z. Xu, J. Lin, Z. Hu, Photovoltaic and solar power forecasting for smart grid energy management, *CSEE J. Power Energy Syst.* 1 (4) (2015) 38–46.
- [4] J. Antonanzas, N. Osorio, R. Escobar, R. Urraca, F. Martinez-de Pison, F. Antonanzas-Torres, Review of photovoltaic power forecasting, *Sol. Energy* 136 (2016) 78–111, <https://doi.org/10.1016/j.solener.2016.06.069>.
- [5] CAISO, Real-time energy market. https://www.caiso.com/Documents/Chapter4_1998AnnualReport_MarketIssuesandPerformance.pdf. (Accessed 25 April 2018).
- [6] G. Box, G. Jenkins, G. Reinsel, Time Series Analysis: Forecasting and Control, Forecasting and Control Series, Prentice Hall, 1994.
- [7] M.T. Hagan, H.B. Demuth, M.H. Beale, et al., Neural Network Design, vol. 20, Pws Pub., Boston, 1996.
- [8] A.J. Smola, B. Schölkopf, A tutorial on support vector regression, *Stat. Comput.* 14 (3) (2004) 199–222.
- [9] J.-S. Jang, Anfis: adaptive-network-based fuzzy inference system, *IEEE Trans. Syst. Man, Cybern.* 23 (3) (1993) 665–685.
- [10] C. Rasmussen, C. Williams, Gaussian Processes for Machine Learning, Adaptive Computation and Machine Learning Series, University Press Group Limited, 2006.
- [11] P. Bacher, H. Madsen, H. Nielsen, Online short-term solar power forecasting, *Sol. Energy* 83 (10) (2009) 1772–1783, <https://doi.org/10.1016/j.solener.2009.05.016>.
- [12] J. Zeng, W. Qiao, Short-term solar power prediction using an RBF neural network, in: IEEE Power and Energy Society General Meeting, 2011, <https://doi.org/10.1109/PES.2011.6039204>.
- [13] H. Pedro, C. Coimbra, Assessment of forecasting techniques for solar power production with no exogenous inputs, *Sol. Energy* 86 (7) (2012) 2017–2028, <https://doi.org/10.1016/j.solener.2012.04.004>.
- [14] M. Bouzerdoum, A. Mellit, A. Massi Pavan, A hybrid model (SARIMA-SVM) for short-term power forecasting of a small-scale grid-connected photovoltaic plant, *Sol. Energy* 98 (PC) (2013) 226–235, <https://doi.org/10.1016/j.solener.2013.10.002>.
- [15] F. Almonacid, P. Pérez-Higueras, E. Fernández, L. Hontoria, A methodology based on dynamic artificial neural network for short-term forecasting of the power output of a PV generator, *Energy Convers. Manag.* 85 (2014) 389–398, <https://doi.org/10.1016/j.enconman.2014.05.090>.
- [16] Y.-K. Wu, C.-R. Chen, H. Abdul Rahman, A novel hybrid model for short-term forecasting in PV power generation, *Int. J. Photoenergy* (2014), <https://doi.org/10.1155/2014/569249>.
- [17] Y. Chu, B. Urquhart, S. Gohari, H. Pedro, J. Kleissl, C. Coimbra, Short-term reforecasting of power output from a 48 MWe solar PV plant, *Sol. Energy* 112 (2015) 68–77, <https://doi.org/10.1016/j.solener.2014.11.017>.
- [18] M. Rana, I. Koprinska, V. Agelidis, Univariate and multivariate methods for very short-term solar photovoltaic power forecasting, *Energy Convers. Manag.* 121 (2016) 380–390, <https://doi.org/10.1016/j.enconman.2016.05.025>.
- [19] V. Sharma, D. Yang, W. Walsh, T. Reindl, Short term solar irradiance forecasting using a mixed wavelet neural network, *Renew. Energy* 90 (2016) 481–492, <https://doi.org/10.1016/j.renene.2016.01.020>.
- [20] V. Kushwaha, N.M. Pindoriya, Very short-term solar pv generation forecast using sarima model: a case study, in: 2017 7th International Conference on Power Systems, ICPS, 2017, pp. 430–435, <https://doi.org/10.1109/ICPS.2017.8387332>.
- [21] A. Asrari, T. Wu, B. Ramos, A hybrid algorithm for short-term solar power prediction - sunshine state case study, *IEEE Trans. Sustain. Energy* 8 (2) (2017) 582–591, <https://doi.org/10.1109/TSTE.2016.2613962>.
- [22] C.-R. Chen, U. Kartini, k-nearest neighbor neural network models for very short-term global solar irradiance forecasting based on meteorological data, *Energies* 10 (2) (2017), <https://doi.org/10.3390/en10020186>.
- [23] A.T. Eseye, J. Zhang, D. Zheng, Short-term photovoltaic solar power forecasting using a hybrid wavelet-pso-svm model based on scada and meteorological information, *Renew. Energy* 118 (2018) 357–367.
- [24] C. Shang, P. Wei, Enhanced support vector regression based forecast engine to predict solar power output, *Renew. Energy* 127 (2018) 269–283.
- [25] Y. Li, Z. Wen, Y. Cao, Y. Tan, D. Sidorov, D. Panasetsky, A combined forecasting approach with model self-adjustment for renewable generations and energy loads in smart community, *Energy* 129 (2017) 216–227.
- [26] D.P. Larson, C.F. Coimbra, Direct power output forecasts from remote sensing image processing, *J. Sol. Energy Eng.* 140 (2) (2018), 021011.
- [27] M.J. Reno, C.W. Hansen, J.S. Stein, Global Horizontal Irradiance Clear Sky Models: Implementation and Analysis, 2012. SANDIA report SAND2012-2389.
- [28] D.P. Larson, L. Nonnenmacher, C.F. Coimbra, Day-ahead forecasting of solar power output from photovoltaic plants in the american southwest, *Renew. Energy* 91 (2016) 11–20, <https://doi.org/10.1016/j.renene.2016.01.039>.

- [29] R.J. Hyndman, G. Athanasopoulos, *Forecasting: Principles and Practice*, 2018. <https://www.otexts.org/fpp>. (Accessed 26 April 2018).
- [30] I. Daubechies, *Ten Lectures on Wavelets*, CBMS-NSF Regional Conference Series in Applied Mathematics, Society for Industrial and Applied Mathematics SIAM, 3600 Market Street, Floor 6, Philadelphia, PA, 1992, 19104.
- [31] D. Percival, A. Walden, *Wavelet Methods for Time Series Analysis*, Cambridge Series in Statistical and Probabilistic Mathematics, Cambridge University Press, 2006.
- [32] B.-L. Zhang, R. Coggins, M. Jabri, D. Dersch, B. Flower, Multiresolution forecasting for futures trading using wavelet decompositions, *IEEE Trans. Neural Netw.* 12 (4) (2001) 765–775, <https://doi.org/10.1109/72.935090>.
- [33] L. Zhang, P. Suganthan, A comprehensive evaluation of random vector functional link networks, *Inf. Sci.* 367–368 (2016) 1094–1105, <https://doi.org/10.1016/j.ins.2015.09.025>.
- [34] H. Peng, F. Long, C. Ding, Feature selection based on mutual information: criteria of max-dependency, max-relevance, and min-redundancy, *IEEE Trans. Pattern Anal. Mach. Intell.* 27 (8) (2005) 1226–1238, <https://doi.org/10.1109/TPAMI.2005.159>.
- [35] J. Arenas-Garcia, A.R. Figueiras-Vidal, A.H. Sayed, Mean-square performance of a convex combination of two adaptive filters, *IEEE Trans. Signal Process.* 54 (3) (2006) 1078–1090, <https://doi.org/10.1109/TSP.2005.863126>.